



Cite this: *Green Chem.*, 2021, **23**, 1212

Electrochemical CO₂ reduction on graphdiyne: a DFT study†

Tianfu Liu,^a Qi Wang,^b  *^b Guoxiong Wang  *^a and Xinhe Bao  ^a

Graphdiyne, a new member of the 2D carbon family, has exhibited interesting physiochemical properties attracting academic attention. Its π -conjugated structure with unique $sp-sp^2$ bonding demonstrates a great potential for electrocatalysis. As electrochemical CO₂ reduction reaction (CO₂RR) has been recognized as a highly promising CO₂ utilization technique, the search for active catalysts is critical for the development of CO₂RR. Herein, using density functional theory calculations, we studied the activity and selectivity of graphdiyne towards CO₂RR. The reaction free energy diagrams are thoroughly investigated, and the results show that the hybridization of $sp-sp^2$ is crucial for high activity owing to the strong adsorption of the *COOH intermediate. Moreover, nitrogen-doping on graphdiyne further improves the activity and selectivity towards CH₃OH and CH₄ products. The lowest limiting potential of CH₃OH on nitrogen-doped graphdiyne is reduced to -0.46 V. The current study predicts the high activity of graphdiyne towards CO₂RR, and illustrates the key role of hybridization on the reactivity of the carbon catalysts.

Received 5th November 2020,

Accepted 8th January 2021

DOI: 10.1039/d0gc03742g

rsc.li/greenchem

Introduction

The electrochemical CO₂ reduction reaction (CO₂RR) possesses enormous potential for CO₂ conversion and utilization since it harnesses electric power for the conversion of CO₂ into useful chemicals and fuels.¹ However, as the CO₂ molecule is extremely stable, the notoriously sluggish kinetics of CO₂RR calls for a highly active cathode catalyst.² Numerous transition metals have been extensively studied as CO₂RR catalysts with different selectivities towards the reduction products.^{3–7} Nonetheless, the metal catalysts suffer from some severe drawbacks, such as low efficiency due to the parasitic hydrogen evolution reaction, poor selectivity, ease of deactivation, and detrimental environmental impact.⁸ Recently, metal-free nanocarbon materials, such as carbon nanotubes, graphene, and nanodiamonds, have demonstrated excellent CO₂RR reactivity higher than or comparable to that of the traditional metal catalysts.^{9–11} The carbon catalysts possess several merits compared with metal catalysts (1) high overpotential for parasitic hydrogen evolution reaction, (2) large active surface area, (3) numerous strain and defect sites tunable for high perform-

ance, and (4) excellent stability.¹² Among numerous carbon materials, carbon nanotubes composed of sp^2 carbon atoms exhibited a low overpotential and high faradaic efficiency towards the CO product,^{12,13} and graphene with the planar sp^2 carbon network demonstrated a high selectivity towards CO and formate products,^{14,15} while the nanodiamond electrode was capable of generating numerous products in the CO₂RR.^{16–18}

It is well known that nanodiamonds and graphenes possessed a network of sp^3 or sp^2 hybridized carbon atoms, respectively.¹⁹ It is recently reported that graphynes with a series of two-dimensional carbon materials were synthesized by a combination of both the sp and sp^2 -hybridized carbon atoms.²⁰ In the graphyne family, graphdiyne, with two diacetylenic linkages between the two carbon hexagon rings, features planar hybrid systems of graphene (sp^2) and carbyne (sp), containing hexagonal rings and acetylenic linkages.²¹ The conjugated π -structures, highly distributed pores, and unique electronic properties of graphdiyne have been attracting considerable attention in the catalytic fields.^{22–25} Therefore, considering the unique electronic structures and surface properties, it is of great interest to study the performance of graphdiyne in the CO₂RR. On the other hand, the relationship between the hybridization of carbon catalysts and their CO₂RR performances has not been thoroughly investigated. The effect of hybridization on the reaction pathway and the product selectivity is still in question. Herein, we studied the activity of graphdiyne in CO₂RR *via* density functional theory (DFT) calculations. It was found that graphdiyne shows excellent activity and selectivity compared with the graphene catalyst, and the

^aState Key Laboratory of Catalysis, Dalian National Laboratory for Clean Energy, Dalian Institute of Chemical Physics, Chinese Academy of Sciences, Dalian, 116023, China. E-mail: wanggx@dicp.ac.cn

^bLiaoning Key Materials Laboratory for Railway, School of Materials and Engineering, Dalian Jiaotong University, Dalian 116028, China. E-mail: qiwang@djtu.edu.cn

†Electronic supplementary information (ESI) available. See DOI: 10.1039/d0gc03742g

carbon atom with $sp-sp^2$ hybridization was identified as the active site. Nitrogen doping is proved to be effective in improving the activity for CH_3OH and CH_4 products, and the investigation of the electronic structure would shed light on the underlying mechanism of CO_2RR on graphdiyne.

Results and discussion

Structure of graphdiyne

The network structure of graphynes could be regarded as the C6 hexagons in graphene interconnected by acetylene linkages, which possessed a special atomic arrangement and an electronic structure.²¹ The two adjacent sp^2 -hybridized carbon atoms in graphdiyne were connected by two “-CEC-” linkages.²² The model of graphdiyne and the bond length of the structure after structural optimization are shown in Fig. 1. It could be observed that the bond length in the benzene ring was around 1.48 Å. The bond lengths in “-CEC-” linkages and the bond linked to the benzene ring were 1.25 Å and 1.47 Å, respectively. Moreover, the two “-CEC-” linkages were connected by a carbon-carbon bond with a bond length of 1.40 Å. The bond length is the essential criteria for the bonding type. When compared with the standard bond length in the benzene ring of 1.39 Å, the benzene ring in graphdiyne was slightly elongated to 1.48 Å. Similarly, the length of the triple bond in acetylene was 1.20 Å; therefore, the triple bond in the “-CEC-” linkage was also elongated to 1.25 Å. It is interesting to note that the bond between the “-CEC-” linkage and the benzene ring exhibited a length of 1.47 Å, which was similar to the C=C bond length in the benzene ring, indicating that a conjugated structure was formed. The two “-CEC-” linkages were connected by a bond of length 1.40 Å, which was shorter than a length of 1.47 Å exhibited by the bond between the “-CEC-” linkage and the benzene ring. Considering the symmetry of the structure, the three carbon atoms are denoted as sites 1, 2, and 3, as shown in Fig. 1. The hybridization of site 1 could be regarded as sp^2 . Moreover, the hybridization of site 2 is between sp^2 and sp ($sp-sp^2$), which was conjugated with the adjacent benzene ring. Site 3 was the one with sp hybridiz-

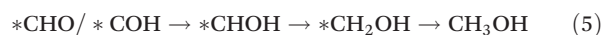
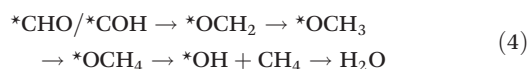
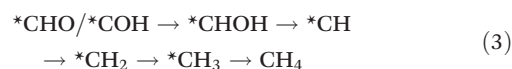
ation. Next, we investigated the free energy diagram of CO_2RR on the sites 1, 2, and 3.

CO_2RR pathway on graphdiyne

For CO_2RR , the two-electron reduction products are CO and HCOOH. As shown in eqn (1) and (2), the initial protonation of CO_2 leads to the generation of either $*COOH$ or $*HCOH$, which can be further reduced to $*CO$ or $*HCOOH$, respectively. Subsequently, $*CO$ and $*HCOOH$ can be desorbed from the catalyst as CO and HCOOH products, respectively.



However, if the adsorbed $*CO$ is further reduced to $*CHO$ or $*COH$, CH_3OH and CH_4 are available as the six-electron or eight-electron reduction products, respectively.



It should be noted that CH_4 can be generated *via* two routes, as shown in eqn (3) and (4). In eqn (3), $*CHO$ or $*COH$ is first reduced to $*CHOH$, which can be further protonated to $*CH$ and H_2O . Then, $*CH$ is further reduced to CH_4 in a series of protonation steps. However, as shown below, the step of $*CHOH \rightarrow *CH$ always involves a high energy barrier compared with $*OCH_3$, which indicates that the pathway in eqn (3) is inferior to that in eqn (4) on graphdiyne. On the other hand, as shown in eqn (4), $*CHO$ is reduced to $*OCH_2$ and further reduced to $*OCH_3$ and again to $*OCH_4$. Next, $*OCH_4$ is reduced to $*OH$ and CH_4 product, which is released from the surface. For CH_3OH , eqn (5) shows the following pathway: $*CHO$ is first reduced to $*CHOH$, and $*CHOH$ is further reduced to $*CH_2OH$, which in turn is reduced to CH_3OH as the final product. The graphical illustration of the pathways is shown in Fig. S1.†

Herein, the computational hydrogen electrode (CHE) model pioneered by Nørskov *et al.* was applied to depict the free energy diagram of CO_2RR , which accounted for the energy of a proton-electron pair ($H^+ + e^-$) in an aqueous solution.²⁶ The reaction free energy of each elementary reaction $-\Delta G$ is calculated as follows:

$$\Delta G = \mu[\text{product}] - \mu[\text{reactant}] - 0.5\mu[H_2(g)] + eU$$

where μ is the chemical potential and U is the applied electrical potential.

Specifically, when $U = 0$ V,

$$\Delta G = -U_L \times e$$

where U_L is the limiting potential of the elementary hydrogenation step.²⁷ Among all the elementary steps, the most negative



Fig. 1 The model of graphdiyne and the related bond lengths in Å.

U_L represented the theoretical limiting potential. Therefore, the limiting potential (U_L) of each specific product (CO, HCOOH, CH₃OH, and CH₄) was obtained by the maximum free energy change, ΔG_{\max} , and then by using the relation $U_L = -\Delta G_{\max}/e$. The step with the ΔG_{\max} is the potential-determining step. The conversion of free energy from the electronic energy and more calculation details are provided in ESI.†

The diagrams of the reaction free energies are plotted in Fig. 2(a)–(c), for sites 1, 2 and 3, respectively. It can be clearly seen that the hydrogenation of CO₂ to form the carboxyl group

(*COOH) is more favourable than that of the formate group (*OCHO). It is noted that *OCHO binds to the active site *via* one of the two oxygen atoms, while *COOH binds *via* the carbon atom.²⁷ The subsequent reduction of *COOH generates *CO, which could either desorb as CO or undergo a further reduction to form *CHO or *COH, which is the key intermediate for CH₃OH and CH₄ products.²⁸ On the other side, the reduction of *OCHO led to the formation of HCOOH, which readily desorbed from the surface of graphdiyne.²⁹ For CO and HCOOH, the formation of *COOH or *OCHO is the step with the highest reaction energy barrier. It is indicated that the first hydrogenation step of CO₂ is the potential-determining step. On sites 1, 2 and 3, the energy barriers of *COOH formation were 1.52 eV, 1.12 eV, and 1.30 eV, respectively. Therefore, the limiting potentials (U_L) for the CO product are -1.52 V, -1.12 V, and -1.30 V, on sites 1, 2, and 3, respectively. For HCOOH, the U_L values were -2.14 V, -1.82 V, and -1.98 V, on sites 1, 2, and 3, respectively. The site 2 on graphdiyne with sp²–sp hybridization exhibits the lowest limiting potential of -1.12 V for the CO product.

As mentioned above, for CH₃OH and CH₄ products, the key intermediate *CHO or *COH is generated from the *CO reduction. This step is crucial for CH₃OH and CH₄ products on numerous catalysts.^{30,31} On graphdiyne, the formation of *CHO is much more favourable than *COH on all three sites. On sites 1, 2 and 3, the free energy changes from *CO to *CHO were 1.04 eV, 0.64 eV, and 0.89 eV, respectively, while the free energy of *COH were 3.84 eV, 3.45 eV, and 3.53 eV, respectively, much higher than that of *CHO. It could be seen that site 2 exhibits the lowest energy barrier for *CO → *CHO. As shown in eqn (3) and (4), for the CH₄ product, the step of *CHOH → *CH₂OH is more favourable than the step of *CHOH → *CH on the three sites. Therefore, the pathway of the CH₄ product is more likely to occur *via* eqn (4). Subsequently, the steps following the formation of *CHO are relatively easy with low energy barriers. Starting from *CHO, on site 1, the step with the largest energy barrier is *CHOH → *CH₂OH with 0.62 eV for CH₃OH, and for CH₄, the step with the largest energy barrier is *OCH₂ → *OCH₃ with 0.48 eV. Similarly, on site 2, for CH₃OH and CH₄ products, the counterparts are *CHO → *CHOH (0.34 eV) and *OCH₂ → *OCH₃ (0.33 eV), respectively. On site 3, for CH₃OH and CH₄ products, the counterparts are *CHO → *CHOH (0.50 eV) and *OCH₂ → *OCH₃ (0.40 eV), respectively. Therefore, starting from *CO for CH₃OH and CH₄ products, the potential-determining step is *CO → *CHO, and the limiting potentials are -1.04 V, -0.64 V, and -0.89 V on sites 1, 2, and 3, respectively. Site 2 is the most active site for both the CH₃OH and CH₄ products. After applying a potential of -1.12 V (U_L for *COOH formation at site 2), the free energy diagram at site 2 is shown in Fig. S2.† At this potential, the free energies of all the intermediates and products moved towards a negative direction. Except for the HCOOH product that still exhibited an energy barrier of 0.7 V, the CO, CH₃OH and CH₄ products demonstrated a downhill energy diagram, indicating that these products are viable at -1.12 V.



Fig. 2 The free energy diagram of CO₂RR on (a) site 1, (b) site 2, and (c) site 3 of graphdiyne.

The major difference among sites 1, 2, and 3 is hybridization. As shown in Fig. S3,† the Bader charge analysis shows that the site 2 changes the hybridization from $sp-sp^2$ to sp^2 , forming a stable conjugated structure with the neighbouring benzene ring, which is beneficial for the charge redistribution. For further insight into the hybridization effect on activity, we investigated the free energy diagram of CO_2RR on graphene, which is purely composed of sp^2 carbon atoms. As shown in Fig. 3, the free energy diagram clearly shows that the step of $CO_2 \rightarrow *COOH$ is the one with the largest energy barrier (2.34 eV) on graphene. Compared with that on graphdiyne, the free energy barrier on graphene is much more difficult to overcome. The enormously high energy barrier on graphene could be attributed to the stable network with the sp^2 hybridized carbon atom, which is detrimental to the activity. On the contrary, a pristine graphdiyne exhibited a high activity towards CO_2RR . The comparison between the graphene and graphdiyne illustrated the key role of hybridization on the activity of carbon catalysts. The $sp-sp^2$ hybridization in graphdiyne is beneficial for the first reduction step of $CO_2 \rightarrow *COOH$ and $*CO \rightarrow *CHO$, which are the key steps for CO_2RR .

The effect of nitrogen doping

The nitrogen doping has been recognized as an effective way to improve the electrochemical performance of carbon materials.^{32,33} The nitrogen dopant induced an alteration in the electronic structure of the catalyst surface, which facilitated the adsorption of intermediates and the electron transfer.³⁴ In CO_2RR , nitrogen had been successfully introduced into the carbon catalysts, leading to a higher activity and selectivity.^{35,36} Herein, we substituted site 1, site 2 or site 3 carbon atom in graphdiyne with a nitrogen atom.

As shown in Fig. 4(a), the nitrogen atom and two neighbouring sites are denoted as N1 to N9 and are investigated as the active sites for CO_2RR . We could learn from pristine graph-



Fig. 3 The free energy diagram of CO_2RR on graphene. Noted that $*COOH$ could not form a stable adsorption structure on graphene. Inset: The graphene model used for the calculations.

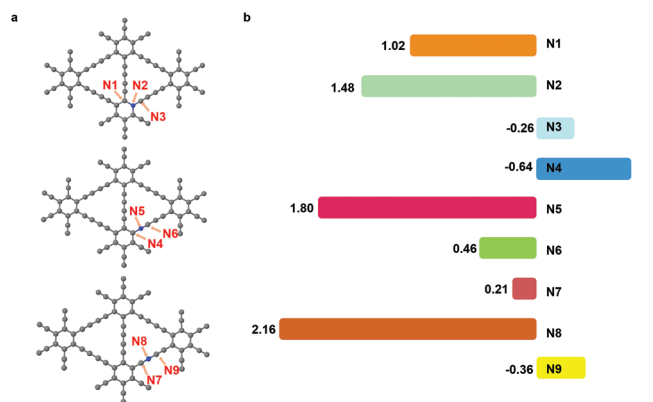


Fig. 4 (a) The structure of graphdiyne with different positions of nitrogen, and the numbers N1–N9 denote the possible active sites. (b) The free energy barrier (eV) of $*COOH$ formation on N1–N9 sites, respectively.

diyne that the first step of $CO_2 \rightarrow *COOH$ is pivotal, which remarkably influenced the overall pathway of CO_2RR . Therefore, we focused on the formation energy of $*COOH$ to screen the catalytic activity of sites N1 to N9. As shown in Fig. 4(b), it can be clearly seen that the free energy of $*COOH$ formation varies significantly on different sites. Notably, N1, N3, N4, N6, N7 and N9 exhibited a low reaction energies of 1.02 eV, -0.26 eV, -0.64 eV, 0.46 eV, 0.21 eV, and -0.36 eV, respectively, for the $*COOH$ formation. Compared with the pristine graphdiyne, the introduction of nitrogen atom is effective in reducing the energy barrier of the $*COOH$ formation.

We further investigated the free energy change along the pathway of CO_2RR on these sites. N3, N4, and N9 exhibited a negative free energy change for the $*COOH$ formation, but further calculations showed that N4 and N9 exhibited a high energy barrier for $*COOH \rightarrow *CO$ of 1.30 eV and 1.68 eV, respectively, while N3 demonstrated a moderate barrier of 0.91 eV. Therefore, we studied the reaction energy profiles of CO_2RR on N1, N3, N6 and N7. As shown in Fig. 5, it can be seen that on N1, the formation of $*COOH$ or $*OCOH$ is the step with the highest energy barriers of 1.02 eV and 1.62 eV, respectively, which is similar to that on the pristine graphdiyne. Next, $*OCOH$ was reduced to HCOOH and desorbed from the catalyst, while $*COOH$ was reduced to $*CO$. Subsequently, $*CO$ could be either desorbed from the surface or reduced to $*CHO$ / $*COH$ and then further reduced to CH_3OH or CH_4 . It was noted that compared with $*CHO$, the $*COH$ formation was much more difficult with a high free energy barrier on N1, N6 and N7. The largest energy barriers from $*CO$ to CH_3OH or CH_4 were 0.65 eV and 0.01 eV in the step of $*CHOH \rightarrow *CH_2OH$ and $*CHO \rightarrow *OCH_2$, respectively. Therefore, the CH_4 product was more favourable than that of CH_3OH on N1.

As for N3, it was interesting to note that the formation of $*COOH$ exhibited a favourable energy change of -0.26 eV, which indicated a strong adsorption of $*COOH$ on N3. From

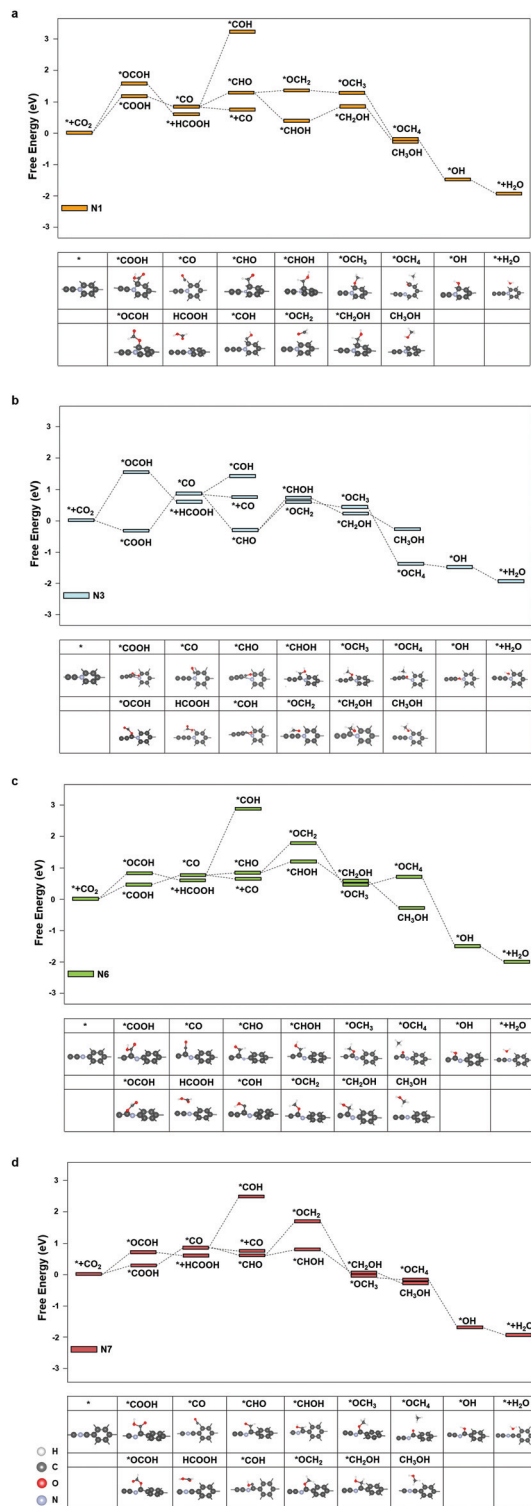


Fig. 5 The free energy diagram of CO₂RR on (a) N1, (b) N3, (c) N6, and (d) N7.

the *COOH configuration in Fig. 5(b), it can be observed that the distance between the carbon atom on the N3 site and the adjacent nitrogen atom is elongated so that a vacancy is formed, in which the *COOH intermediate is trapped.

However, the step of *COOH → *CO exhibited a high energy barrier of 0.91 eV. Subsequently, the energy barriers of *CO → *CHOH and *CO → *OCH₂ are 1.07 eV and 1.03 eV, respectively, which indicated that CH₃OH and CH₄ were less likely to generate than the CO product. Therefore, it was observed that the CO production was more dominant on N3.

As shown in Fig. 5(c) and (d), on N6 and N7, the energy barriers of the *COOH formation are 0.46 eV and 0.21 eV, respectively. Hence, the formation of *COOH is not the step with the largest energy barrier on N7. Instead, the step of *COOH → *CO exhibited high energy barriers of 0.60 eV. In the following steps, compared with that of the pristine graphdiyne and N1, the energy barrier of *CO → *CHO was significantly reduced, which was beneficial for the CH₃OH and CH₄ products. Starting from *CO, the largest energy barriers for CH₃OH and CH₄ products were 0.26 eV and 0.98 eV on N6, respectively, while the counterparts on N7 were 0.02 eV and 1.00 eV, respectively. It was clearly seen that the CH₄ production was impeded by the sluggish step of *CHO → *OCH₂, while the steps towards the CH₃OH product was greatly facilitated on N6 and N7. Fig. S4† shows the free energy diagram of CO₂RR on N1, N3, N6, and N7 at applied potentials of −1.02 V, −0.91 V, −0.46 V and −0.60 V, respectively. It could be seen that on N6, the pathway to CH₃OH was energetically favourable at a low potential of −0.46 V. Nitrogen-doping not only improved the activity of CO₂RR by reducing the energy barrier of the *COOH formation, but also enhanced the selectivity towards CH₄ on N1, CO on N3, and CH₃OH on N6 and N7, respectively. N6 exhibited the lowest limiting potential of −0.46 V for the CH₃OH product. It indicated that the nitrogen-doped graphdiyne possessed a high activity and selectivity towards CH₃OH, a valued liquid fuel, which was reportedly only produced on metal catalysts, such as Cu-based catalysts and cobalt phthalocyanine in literature.^{37–39}

The nitrogen defects and hydrogen evolution reaction

It has been reported that the nitrogen-defects are crucial for the CO₂RR activity.^{15,16,19} Herein, the pyrrolic and pyridinic nitrogen defects were constructed on graphdiyne to investigate the activity of nitrogen defects. As shown in Fig. S6,† the first hydrogenation step is more favoured towards *COOH instead of *OCOH on both the nitrogen defects. Subsequently, it is interesting to note that the adsorption of *CO is stable on the pyrrolic nitrogen, and the following hydrogenation step of *CO → *CHOH was energetically easier in occurrence than the desorption of *CO. On the other hand, on the pyridinic nitrogen *CO is readily desorbed from the catalyst. The primary reduction product on the pyrrolic nitrogen is CH₃OH, and the highest energy barrier is 1.29 eV on the step of *CH₂OH → *CH₃OH. On the pyridinic nitrogen, CO is the primary product with the highest energy barrier of 0.96 eV on the step of *COOH → *CO. It could be seen that on comparison with the pyrrolic nitrogen the pyridinic nitrogen is more active and favourable for the CO product. This is consistent with previous studies on the nitrogen-doped carbon catalysts for CO₂RR.^{40–42}

The hydrogen evolution reaction (HER) is a competitive reaction for CO₂RR, which should be avoided. The free energy of *H adsorption is studied on sites 1, 2, 3, and N1–N9. As shown in Fig. S7,† the results indicate that the adsorption energy of *H is relatively more negative than the formation of *COOH, as shown in Fig. 2 and 5, except for N3 site, which indicates that H* adsorption is strong on these sites. On the N3 site, the free energy change of CO₂ → *COOH is −0.26 eV, while the *H adsorption energy is 0.02 eV. Thus, the N3 site is selective towards CO₂RR against HER. The results implied that HER could be a concerning issue for the practical usage of the graphdiyne catalyst for CO₂RR. Nonetheless, it should be noted that in recent experimental studies on CO₂RR, numerous methods were employed to suppress HER effectively, such as ionic liquids,⁴³ aqueous pH buffer regions,⁴⁴ cations,⁴⁵ and nitrogen co-catalysts.⁴⁶ In particular, the flow cell equipped with a gas diffusion electrode allowed the alkaline electrolyte use to suppress HER, which significantly enhanced the faradaic efficiency of CO₂RR products.^{47–49} Using these methods, some metals, such as Pd, which were theoretically inclined to produce H₂, exhibited a high faradaic efficiency for CO₂RR.^{50,51} Therefore, by taking cautious approaches, the parasitic HER on graphdiyne could be dealt with in CO₂RR experiments.

The electronic structures: effects of hybridization and doping

To further explore the mechanism of CO₂RR on pristine and nitrogen-doped graphdiyne, we studied the partial density of states (PDOS) of the carbon 2p orbital in sites 1, 2, and 3 of pristine graphdiyne and N1, N3, N6, and N7 in nitrogen-doped graphdiyne. It was reported that the stronger states near the Fermi level indicated a better capacity for the electron-transfer, therefore facilitating the catalytic activity. As shown in Fig. 6(a), on site 1 and site 3 of pristine graphdiyne, the states near the Fermi level are relatively low. Compared with site 1 and site 3, site 2 showed higher states near the Fermi level. As discussed in the energy diagram of CO₂RR, the formation of

*COOH is much easier on site 2 compared with that on site 1 and site 3. Similarly, in the nitrogen-doped graphdiyne, the states near the Fermi level were much higher in N6 and N7 than that observed in N1 and N3, which were consistent with the low energy barrier of *CO → *CHO on N6 and N7. The favourable energy change of the formation of *COOH and *CHO on N3 could be attributed to the elongation between the active site and the adjacent carbon atom, which led to a vacancy accommodating the intermediate. As shown in Fig. S6,† the charge density difference of the *COOH adsorption on pristine and nitrogen-doped graphdiyne shows that the site 2 in pristine graphdiyne, along with N6 and N7 in the nitrogen-doped graphdiyne, exhibits a significant alteration in the charge density of the catalyst, with a noticeable hybridized conjugation on the active site and adjacent atoms. Moreover, as mentioned above, the Bader analysis indicated that the lower free energy barrier for the *COOH formation was closely related to the hybridization transition of the sp²–sp² to sp². The PDOS and charge analysis suggested that site 2, N6 and N7 possessed a better capability of charge transfers, which explained the lower energy barrier of the *COOH and *CHO formations on these sites.

Conclusion

Using the DFT calculations, the activity and selectivity of graphdiyne towards CO₂RR were evaluated, and the effect of carbon hybridization was also thoroughly investigated. The results showed that the site 2 with sp²–sp hybridization exhibited the best activity with a low activation barrier for the CO, CH₃OH and CH₄ products. Compared with graphene with pure sp² hybridization that showed a much higher energy barrier for CO₂RR, the sp²–sp hybridization with the conjugated structure was crucial for the CO₂RR activity over graphdiyne. Nitrogen doping was found to be effective for improving the CO₂RR activity. The electronic structure analysis demonstrates that the strong adsorption of key intermediate *COOH/*CHO could be attributed to the increased density of states near the Fermi level and the conjugated charge redistribution facilitated the sp²–sp to sp² transition, leading to a stronger adsorption of the intermediates. The current study predicts a good application prospect of graphdiyne for CO₂RR, and the new insight into the relationship between hybridization and reactivity sheds light on further development of the carbon catalysts for CO₂RR.

Conflicts of interest

The authors declare no competing financial interest.

Acknowledgements

We gratefully acknowledge the financial support from the National Natural Science Foundation of China (grant no.

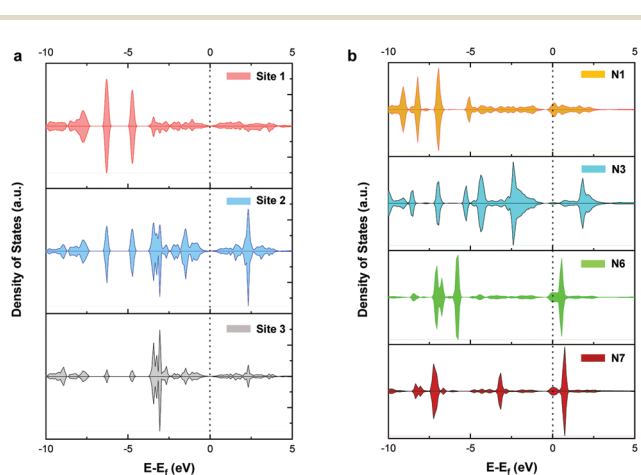


Fig. 6 Partial density of states (PDOS) of the carbon 2p orbital of (a) sites 1, 2, and 3 in pristine graphdiyne and (b) N1, N3, N6, and N7 in nitrogen-doped graphdiyne. The dashed line refers to the Fermi level.

22002158 and 21403023), the National Scientific Fund of Liaoning Province (grant no. 20180510035), and the Dalian National Laboratory for Clean Energy (grant no. DNL180404 and DNL201924). G. X. Wang thanks the financial support from the CAS Youth Innovation Promotion (grant no. Y201938). T. F. Liu thanks the fellowship of China Postdoctoral Science Foundation (grant no. 2019M661142).

Notes and references

- S. Zhang, Q. Fan, R. Xia and T. J. Meyer, *Acc. Chem. Res.*, 2020, **53**, 255–264.
- S. Nitopi, E. Bertheussen, S. B. Scott, X. Liu, A. K. Engstfeld, S. Horch, B. Seger, I. E. L. Stephens, K. Chan, C. Hahn, J. K. Nørskov, T. F. Jaramillo and I. Chorkendorff, *Chem. Rev.*, 2019, **119**, 7610–7672.
- D. H. Nam, P. De Luna, A. Rosas-Hernandez, A. Thevenon, F. Li, T. Agapie, J. C. Peters, O. Shekhah, M. Eddaoudi and E. H. Sargent, *Nat. Mater.*, 2020, **19**, 266–276.
- Y. Wu, Z. Jiang, X. Lu, Y. Liang and H. Wang, *Nature*, 2019, **575**, 639–642.
- W. Ma, S. Xie, T. Liu, Q. Fan, J. Ye, F. Sun, Z. Jiang, Q. Zhang, J. Cheng and Y. Wang, *Nat. Catal.*, 2020, **3**, 478–487.
- K. Ye, A. Cao, J. Shao, G. Wang, R. Si, N. Ta, J. Xiao and G. Wang, *Sci. Bull.*, 2020, **9**, 711–719.
- D. Gao, H. Zhou, J. Wang, S. Miao, F. Yang, G. Wang, J. Wang and X. Bao, *J. Am. Chem. Soc.*, 2015, **137**, 4288–4291.
- B. Pan, X. Zhu, Y. Wu, T. Liu, X. Bi, K. Feng, N. Han, J. Zhong, J. Lu, Y. Li and Y. Li, *Adv. Sci.*, 2020, **7**, 2001002.
- D. Yang, L. Liu, Q. Zhang, Y. Shi, Y. Zhou, C. Liu, F. Wang and X. Xia, *Sci. Bull.*, 2020, **65**, 796–802.
- P. Zhu and H. Wang, *Sci. Bull.*, 2020, **65**, 977–979.
- W. Li, M. Seredych, E. Rodríguez-Castellón and T. J. Bandosz, *ChemSusChem*, 2016, **9**, 606–616.
- A. Vasileff, Y. Zheng and S. Z. Qiao, *Adv. Energy Mater.*, 2017, **7**, 1700759.
- S. Chen, T. Liu, S. O. Olanrele, Z. Lian, C. Si, Z. Chen and B. Li, *J. Energy Chem.*, 2021, **54**, 143–150.
- N. Sreekanth, M. A. Nazrulla, T. V. Vineesh, K. Sailaja and K. L. Phani, *Chem. Commun.*, 2015, **51**, 16061–16064.
- H. Wang, Y. Chen, X. Hou, C. Ma and T. Tan, *Green Chem.*, 2016, **18**, 3250–3256.
- Y. Liu, S. Chen, X. Quan and H. Yu, *J. Am. Chem. Soc.*, 2015, **137**, 11631–11636.
- T. Liu, S. Ali, Z. Lian, C. Si, D. S. Su and B. Li, *J. Mater. Chem. A*, 2018, **6**, 19998–20004.
- K. Nakata, T. Ozaki, C. Terashima, A. Fujishima and Y. Einaga, *Angew. Chem., Int. Ed.*, 2014, **53**, 871–874.
- X. Duan, J. Xu, Z. Wei, J. Ma, S. Guo, S. Wang, H. Liu and S. Dou, *Adv. Mater.*, 2017, **29**, 1701784.
- G. Li, Y. Li, H. Liu, Y. Guo, Y. Li and D. Zhu, *Chem. Commun.*, 2010, **46**, 3256–3258.
- C. Huang, Y. Li, N. Wang, Y. Xue, Z. Zuo, H. Liu and Y. Li, *Chem. Rev.*, 2018, **118**, 7744–7803.
- X. Gao, H. Liu, D. Wang and J. Zhang, *Chem. Soc. Rev.*, 2019, **48**, 908–936.
- Y. Zhao, J. Wan, H. Yao, L. Zhang, K. Lin, L. Wang, N. Yang, D. Liu, L. Song, J. Zhu, L. Gu, L. Liu, H. Zhao, Y. Li and D. Wang, *Nat. Chem.*, 2018, **10**, 924–931.
- L. Yang, J. Shui, L. Du, Y. Shao, J. Liu, L. Dai and Z. Hu, *Adv. Mater.*, 2019, **31**, e1804799.
- L. Hui, Y. Xue, H. Yu, Y. Liu, Y. Fang, C. Xing, B. Huang and Y. Li, *J. Am. Chem. Soc.*, 2019, **141**, 10677–10683.
- A. A. Peterson, F. Abild-Pedersen, F. Studt, J. Rossmeisl and J. K. Nørskov, *Energy Environ. Sci.*, 2010, **3**, 1311.
- S. Back, J. Lim, N. Y. Kim, Y. H. Kim and Y. Jung, *Chem. Sci.*, 2017, **8**, 1090–1096.
- S. Back and Y. Jung, *ACS Energy Lett.*, 2017, **2**, 969–975.
- J. T. Feaster, C. Shi, E. R. Cave, T. Hatsukade, D. N. Abram, K. P. Kuhl, C. Hahn, J. K. Nørskov and T. F. Jaramillo, *ACS Catal.*, 2017, **7**, 4822–4827.
- S. Wang, J. Wang and H. Xin, *Green Energy Environ.*, 2017, **2**, 168–171.
- T. Liu, S. Ali, Z. Lian, B. Li and D. S. Su, *J. Mater. Chem. A*, 2017, **5**, 21596–21603.
- C. Chen, X. Sun, X. Yan, Y. Wu, H. Liu, Q. Zhu, B. B. A. Bediako and B. Han, *Angew. Chem.*, 2020, **59**, 11123–11129.
- T. Ma, Q. Fan, X. Li, J. Qiu, T. Wu and Z. Sun, *J. CO₂ Util.*, 2019, **30**, 168–182.
- G. Li, Y. Qin, Y. Wu, L. Pei, Q. Hu, H. Yang, Q. Zhang, J. Liu and C. He, *Chin. J. Catal.*, 2020, **41**, 830–838.
- H. Wang, J. Jia, P. Song, Q. Wang, D. Li, S. Min, C. Qian, L. Wang, Y. F. Li, C. Ma, T. Wu, J. Yuan, M. Antonietti and G. A. Ozin, *Angew. Chem., Int. Ed.*, 2017, **27**, 7955–7960.
- Y. Song, W. Chen, C. Zhao, S. Li, W. Wei and Y. Sun, *Angew. Chem., Int. Ed.*, 2017, **36**, 10980–10984.
- J. Albo and A. Irabien, *J. Catal.*, 2016, **343**, 232–239.
- W. Zhang, Q. Qin, L. Dai, R. Qin, X. Zhao, X. Chen, D. Ou, J. Chen, T. Chuong, B. Wu and N. Zheng, *Angew. Chem., Int. Ed.*, 2018, **57**, 9475–9479.
- Y. Wu, Z. Jiang, X. Lu, Y. Liang and H. Wang, *Nature*, 2019, **575**, 639–642.
- J. Wu, R. M. Yadav, M. Liu, P. P. Sharma, C. S. Tiwary, L. Ma, X. Zou, X. Zhou, B. I. Yakobson, J. Lou and P. M. Ajayan, *ACS Nano*, 2015, **9**, 5364–5371.
- H. Wang, Y. Chen, X. Hou, C. Ma and T. Tan, *Green Chem.*, 2016, **18**, 3250–3256.
- S. Liu, H. Yang, X. Huang, L. Liu, W. Cai, J. Gao, X. Li, T. Zhang, Y. Huang and B. Liu, *Adv. Funct. Mater.*, 2018, **28**, 1800499.
- B. A. Rosen, A. Salehi-Khojin, M. R. Thorson, W. Zhu, D. T. Whipple, P. J. A. Kenis and R. I. Masel, *Science*, 2011, **334**, 643–644.
- C. Delacourt, P. L. Ridgway, J. B. Kerr and J. Newman, *J. Electrochem. Soc.*, 2008, **155**, B42–B49.
- M. R. Thorson, K. I. Siil and P. J. A. Kenis, *J. Electrochem. Soc.*, 2013, **160**, F69–F74.

- 46 C. E. Tornow, M. R. Thorson, S. Ma, A. A. Gewirth and P. J. A. Kenis, *J. Am. Chem. Soc.*, 2012, **134**, 19520–19523.
- 47 Q. Gong, P. Ding, M. Xu, X. Zhu, M. Wang, J. Deng, Q. Ma, N. Han, Y. Zhu, J. Lu, Z. Feng, Y. Li, W. Zhou and Y. Li, *Nat. Commun.*, 2019, **10**, 2087.
- 48 X. Lu, Y. Wu, X. Yuan, L. Huang, Z. Wu, J. Xuan, Y. Wang and H. Wang, *ACS Energy Lett.*, 2018, **3**, 2527–2532.
- 49 K. Ye, Z. Zhou, J. Shao, L. Lin, D. Gao, N. Ta, R. Si, G. Wang and X. Bao, *Angew. Chem.*, 2020, **59**, 4814–4821.
- 50 D. Gao, H. Zhou, F. Cai, J. Wang, G. Wang and X. Bao, *ACS Catal.*, 2018, **8**, 1510–1519.
- 51 B. M. Tackett, J. H. Lee and J. G. Chen, *Acc. Chem. Res.*, 2020, **53**, 1535–1544.